41st AIAA Fluid Dynamics Conference and Exhibit
27 - 30 June 2011, Honolulu, Hawaii

AIAA 2011-3872

Transition Research with Temperature-Sensitive Paints in the Boeing/AFOSR Mach-6 Quiet Tunnel

Amanda Chou*, Christopher A. C. Ward*, Laura E. Letterman*, and Ryan P. K. Luersen*
Purdue University, West Lafayette, IN, 47907

Matthew P. Borg†
Air Vehicles Directorate, Air Force Research Laboratory, Wright-Patterson AFB, OH

Steven P. Schneider‡
Purdue University, West Lafayette, IN, 47907

The Boeing/AFOSR Mach-6 Quiet Tunnel (BAM6QT) is used for the study of noise effects on transition. A 12-inch ball valve was installed in the BAM6QT in April 2011, replacing a slow gate valve. This ball valve allows the tunnel to run without the use of diaphragms, though experiments are still typically run with the double burst diaphragm system. Four projects in the BAM6QT are also described in this paper. The first project tested a method of calibrating temperature-sensitive paints using Schmidt-Boelter heat transfer gauges. A 7-deg half-angle cone was tested at 0-deg angle of attack and compared to theory. The second project tested two von Karman ogive models. On the 7.62-cm-diameter ogive model at 0-deg angle of attack, the flow remained laminar for a smooth nosetip, a nosetip with a two-dimensional roughness strip, and a nosetip with distributed roughness. Isolated roughness elements larger than 51 μm cause transition on this model at higher Reynolds numbers. A smaller 5.08-cm-diameter ogive model was constructed to allow the model to start at 2-deg angle of attack and to prevent a reflected bow shock from impinging on the model. Transition occurred on the lee ray on the smaller model. Forward-facing and aft-facing steps on the model nosetip did not appear to affect transition. Third, a 3-m circular-arc flared cone was run in different axial positions in the tunnel to determine if there was an effect. Sensors were also installed aft of the model to try to measure noise levels with an installed model in an attempt to show that transition occurs on the cone in fully quiet flow. For the last project, roughness dots were added to the same flared cone in an attempt to change vortex spacing. The flared cone remains a subject for future research.

Nomenclature

D	diameter of roughness dots
k	thermal conductivity
L	thickness of insulation layer
N	amplification factor
p	pressure
$\dot{q}$	heat flux
Re	Reynolds number based on freestream conditions
t	time after tunnel start
T	temperature
ΔT	change in temperature
x	distance from model nosetip
z	distance from tunnel throat

Subscript

0	at stagnation conditions
∞	at freestream conditions
i	at initial conditions
s	on the surface
ref	for model before run start

*Research Assistant, AIAA Student Member
†Booz Allen Hamilton, AIAA Member
‡Professor, Associate Fellow AIAA

Copyright © 2011 by Steven P. Schneider. Published by the American Institute of Aeronautics and Astronautics, Inc., with permission.

model	for the model during the run
nose	for nosetip of the model, $x = 0$

Abbreviations

A/D	analog-to-digital
BAM6QT	Boeing/AFOSR Mach-6 Quiet Tunnel
PIHF	Pipe-insert hot film
RMS	root-mean-square
SB	Schmidt-Boelter (heat transfer gauge)
TSP	temperature-sensitive paint

I. Introduction

A. Hypersonic Laminar-Turbulent Transition

Laminar-turbulent transition in hypersonic boundary layers is a topic of particular interest. The uncertainty in predicting the nature of transition and the great effect it has on heat transfer, skin friction, aero-optical distortion, etc. affects the design of hypersonic vehicles. Without an understanding of transition and its mechanisms, many hypersonic vehicles run the risk of being over-designed.[1] An inability to adequately predict transition requires vehicles to be designed to withstand a "worst-case scenario." This usually requires excess thermal protection and thus creates heavier, less-efficient vehicles. Some hypersonic missions can be pursued with acceptable risk only if transition can be better understood and better controlled.

Some of the uncertainty involved in transition prediction is because much of the ground testing is done in conventional facilities. The noise levels of these conventional wind tunnels are on the order of 1% of the mean pressure or greater. Conventional facilities usually have turbulent boundary layers on their nozzle walls, which radiate noise into the freestream. These higher freestream noise levels can cause transition to occur earlier than in a quiet environment, such as flight.[2–4]

B. The Boeing/AFOSR Mach-6 Quiet Tunnel

Quiet tunnels have much lower noise levels than conventional wind tunnels. The freestream noise level of a quiet tunnel is about 0.1% or less.[2] The use of such tunnels to study the nature of transition provides insight into transition in a quiet, flight-like condition. Purdue University's Boeing/AFOSR Mach-6 Quiet Tunnel (BAM6QT) is one of two operational hypersonic quiet tunnels. NASA Langley's former Mach-6 quiet tunnel is now operational at Texas A&M.[5]

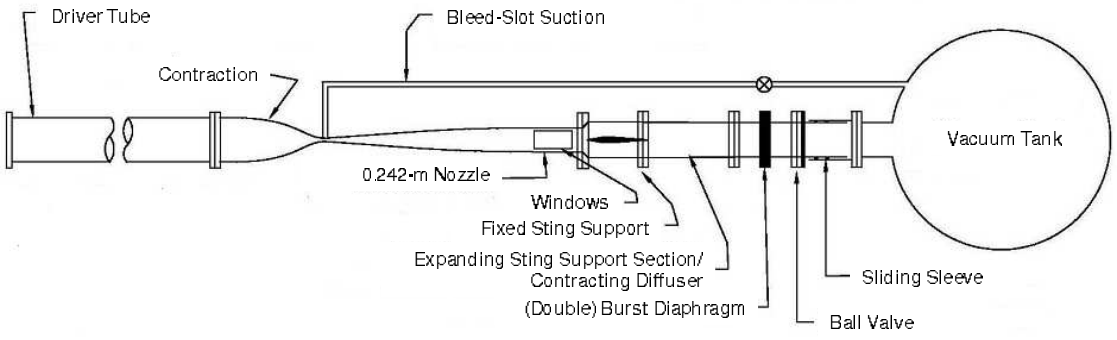

Figure 1. A schematic of the Boeing/AFOSR Mach-6 Quiet Tunnel.

Purdue's BAM6QT was designed as a Ludwieg tube in order to reduce the cost of running the tunnel while providing higher Reynolds numbers. The Ludwieg tube involves a long pipe, a converging-diverging nozzle, test section, diffuser, double burst diaphragms, and a vacuum tank (Figure 1). The tunnel is run by pressurizing the driver tube to a desired stagnation pressure and pumping the downstream portion to vacuum. Bursting the diaphragms starts the flow, which sends a shock wave downstream into the vacuum tank and an expansion wave upstream. The expansion wave reflects between the contraction and the upstream end of the driver tube every 0.2 s throughout the length of the run, causing the stagnation pressure to drop quasi-statically in a stair-step fashion.

In the BAM6QT's quiet configuration, air is bled from the throat of the nozzle using a fast valve, allowing a new boundary layer to grow on the divergent portion of the nozzle wall. This configuration is referred to as

a "bleeds open" configuration. The extended length and high polish of the nozzle allows the boundary layer to remain laminar to fairly high stagnation pressures. To run the tunnel in a conventional configuration, the bleed valves are closed and the boundary layer is allowed to grow naturally on the nozzle wall. The nozzle-wall boundary layer is usually turbulent in the conventional configuration.

A pipe insert and extension[6] (Figure 2) is also used to take advantage of the sudden increase in diameter in the diffuser. Aft of the nozzle exit, the diffuser expands from a 24.1-cm (9.5-in.) diameter to a 35.9-cm (14.125-in.) diameter via a 45° angle.[7] This insert can be slid backward in the diffuser section or "opened" to create an annular gap, through which suction may occur.[8] The use of this gap was originally intended as a form of shock-boundary-layer control but is also used as a method of controlling nozzle-wall boundary-layer separation. A 9.5-mm (3/8-in.) gap is typically used to reduce nozzle-wall boundary-layer separation for larger models.

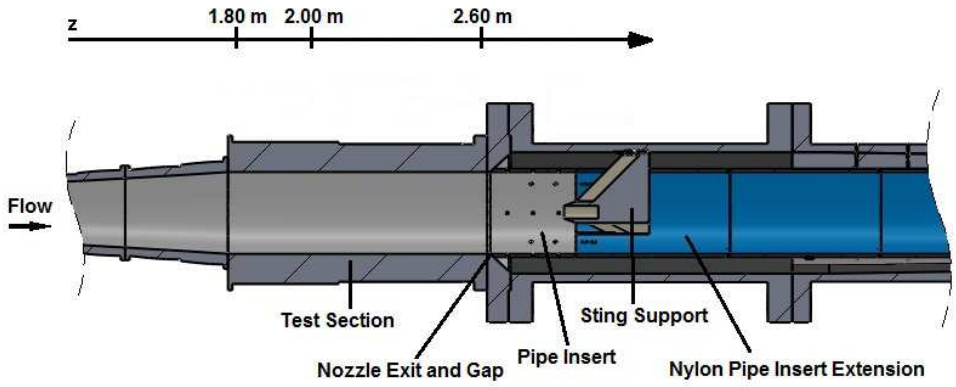

Figure 2. A schematic of the inside of the Boeing/AFOSR Mach-6 Quiet Tunnel highlighting the pipe insert and extension.

1. Installation of a 12-Inch Ball Valve

A slow gate valve was originally used to separate the upstream and downstream portions of the tunnel so that diaphragms could be installed after each run without filling the vacuum tank back to atmospheric pressure. Burst diaphragms occasionally got stuck in the gate valve as much as 25% of the time. The seal in the gate valve was starting to degrade as the seating surfaces were wearing out. A 12-in. Jamesbury 9300 ball valve with a pneumatic actuator was installed in the BAM6QT in April 2011 to replace this gate valve. The gaps present inside the ball valve are both shallower and narrower than the seat for the disk in the gate valve, so diaphragms are less likely to get stuck in the ball valve. The ball valve also seals better and opens faster, so it provides more efficiency and makes it possible for the BAM6QT to run without the use of diaphragms.

Several recent experiments required the BAM6QT be run at pressures for which there are currently no suitable diaphragms. It was hoped that, with the use of the ball valve, the tunnel could be properly started with no diaphragms installed. Several noisy runs with initial stagnation pressures of 45-65 psia were successfully started using only the ball valve. One run at 45 psia was also started using diaphragms in order to compare starting characteristics and to ensure that quality flow was obtained when starting the tunnel with the ball valve. Additionally, one quiet run with an initial stagnation pressure of 146 psia was started using only the ball valve.

Figures 3(a) and (b) show the uncalibrated output of a hot film mounted on the nozzle wall at $z = 1.892$ m for quiet and noisy runs started in both the traditional manner with diaphragms and with only the new ball valve. Here, z is the distance from the nozzle throat. For both the low-pressure noisy and high-pressure quiet cases, it is clear that the start-up process takes somewhat longer when using the ball valve than it does when using diaphragms. This is not unexpected since the initial expansion that travels upstream through the nozzle and initiates the flow is probably smoothed out during the approximately 2 s it takes the ball valve to open. When diaphragms are used to start the tunnel, the expansion is a much more sudden process. For the quiet case, the run also terminates about 1 s earlier when started with the ball valve than when diaphragms are used. In the noisy case, the length of the run is also shortened by an undetermined amount since the end of the run that was started with diaphragms was not recorded.

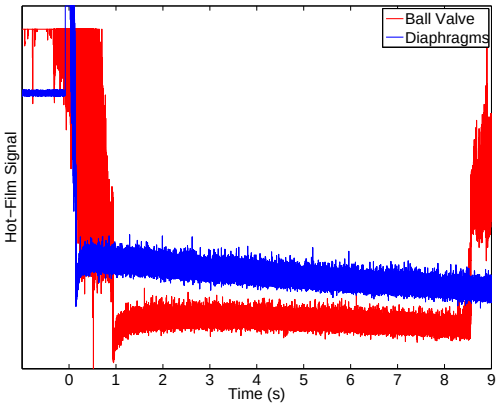

(a) Nozzle-wall hot-film traces, noisy runs, $p_{0,i}$ ≈45 psia

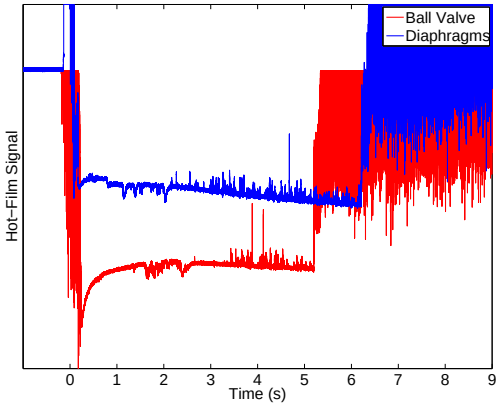

(b) Nozzle-wall hot-film traces, quiet runs, $p_{0,i}$ ≈145 psia

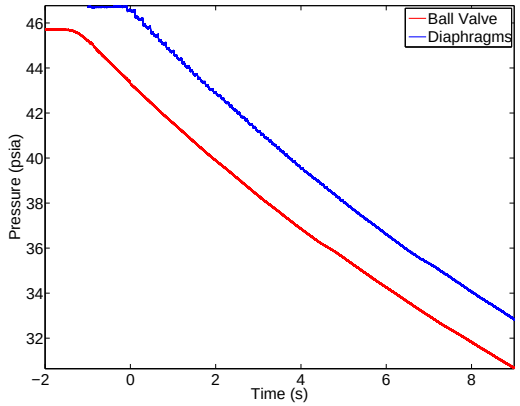

(c) Contraction-entrance pressure, noisy runs, $p_{0,i}$ ≈45 psia

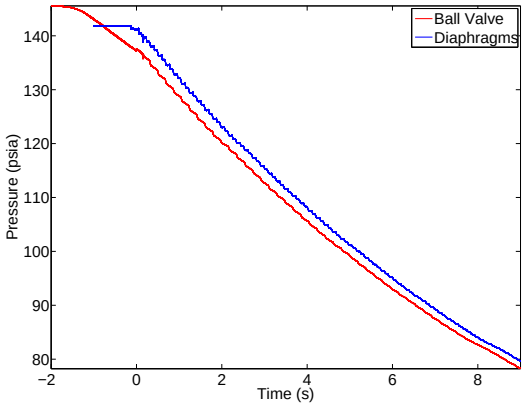

(d) Contraction-entrance pressure, quiet runs, $p_{0,i}$ ≈145 psia

Figure 3. Nozzle-wall hot film and contraction-entrance pressure traces for noisy and quiet runs started with diaphragms and the new ball valve. Hot film is located at z = 1.892 m.

The tunnel stagnation pressure (Figures 3(c) and (d)) are also shown for both cases. The diaphragm/ball-valve run pairs did not start at identical pressures, thus adding a little ambiguity to a direct comparison. Nevertheless, the average slope of the pressure drop is approximately the same when comparing runs with similar conditions that started in different manners. Of note is the lack of the characteristic "stair-step" in the noisy ball-valve case. Here, the expansion wave has evidently been smoothed out to the point that the head and tail passages cannot be discerned. Thus, the noisy ball-valve case here lacks the ostensibly quasi-steady 0.2 s conditions that are evident when starting with diaphragms. For the quiet case, a "stair-step" pattern is observed when starting with the ball valve. However, between expansion head and tail reflection, the conditions are not quasi-steady, but rather decrease linearly in the 0.2 s time between expansion reflections.

Although quasi-steady conditions are not achieved when starting the BAM6QT with the ball valve, it appears that the tunnel can indeed be started in this manner and provides a reasonable length of usable flow time. It seems likely that, in the very least, the ball valve can be used to start the tunnel for pressures for which there are no suitable diaphragms. At best, this method may eliminate the need to use diaphragms in the future.

2. Experiments in the BAM6QT

Four of the current experiments done in the BAM6QT are described in this paper. The first experiment aims to validate a method of providing qualitative heat transfer for temperature-sensitive paints. In the second experiment, two von Karman ogives were created to study nosetip roughness effects on transition. The third

and fourth experiments involve the same flared cone model discussed in References 9 and 10. The third experiment attempts to show transition in fully quiet flow on a flared cone. The last experiment investigates the use of roughness elements to change spacing of streamwise vortices on the flared cone.

II. Extracting Quantitative Heat Transfer from Temperature-Sensitive Paint

A. Description of Procedure

Obtaining quantitative heat transfer was one of the original goals of the development of temperature-sensitive paints (TSP) for studies in the BAM6QT.[11] The development and use of TSP is detailed in Reference 12. The method currently used at Purdue University involves painting an aluminum model with a thin insulating layer of white paint. The insulating layer consists of LustreKote white primer and "Jet White" spray paint. The temperature-sensitive paint consists of the luminophore molecule Ru(Bpy) mixed in Limco LC4000 clearcoat and LHM medium hardener. Four layers of this temperature-sensitive paint are applied to the model on top of the insulating layers using an airbrush paint gun.

A method was devised by Dr. John P. Sullivan of Purdue University to calibrate the TSP using data from Schmidt-Boelter (SB) heat transfer gauges.[13] A square patch of TSP is compared to the SB gauge. Ideally, the patch of TSP should be in a location where the heat transfer rate is the same as measured by the SB gauge. This is not always a trivial task especially when dealing with a three-dimensional flowfield. The local heat flux can be found using Fourier's law

$$\dot{q} = -k\nabla T \tag{1}$$

where $\dot{q}$ is the local heat flux and k is the thermal conductivity of the substrate, or the model. Several assumptions need to be made to simplify Equation 1. It is assumed that the heat transfer is one-dimensional (in the radial direction). It is also assumed that the temperature profile in the radial direction across the insulating layer is linear. Finally, the temperature at the base of the insulator (model temperature, T_{model}) is assumed to be constant throughout a run. This constant model temperature assumption was found to be accurate to within roughly 4%.[14] Fourier's law can then be simplified to the following linear equation, incorporating the finite thickness of the insulating paint layer,

$$\dot{q} = \frac{k}{L}(T - T_{\text{model}}) \tag{2}$$

where L is the thickness of the insulating layer and T is the temperature of the surface during the run obtained from the TSP. Finally, Equation 2 can be modified to include ΔT since all the TSP images can be calibrated to give ΔT,

$$\dot{q} = \frac{k}{L}(\Delta T + T_{ref} - T_{\text{model}}) \tag{3}$$

$$\Delta T = T - T_{ref} \tag{4}$$

where T_{ref} is the temperature of the model surface just before the run starts. The method of extracting heat transfer from the TSP works by iterating T_{model} and k/L until good agreement is found between the TSP and a SB gauge on the model. A least-squares method was employed to find values for the two constants that produced the best fit between the calibrated TSP and the SB readings. According to the definitions of T_{model} and T_{ref} and the assumption of a constant model temperature during a run, these two temperatures should be nominally the same. However, T_{model} was chosen to best fit the data, regardless of how much it varies from T_{ref}.

There are some inherent issues involved with obtaining quantitative heat transfer from the TSP in the BAM6QT. During tunnel startup, the model experiences significant heating. This large impulse of heating is thought to dissipate through the aluminum model before the run starts, but it's possible that the TSP might show some residual heating. The residual heating, if present, would cause problems in obtaining accurate heat transfer from the TSP. The low heat transfer in the BAM6QT also presents a problem. It may be difficult to obtain a good calibration if the range of heat transfer is so low.

B. Results

The first set of experiments to test the validity of the heat-transfer data-reduction procedure were completed in January 2011. Tests were performed on a nominally sharp 7° half-angle cone at zero degrees angle of attack. Six SB gauges were installed in the model, with the axial locations and the serial numbers of the gauges shown in Table 1. The installed sensors in Table 1 were Medtherm 8-2-0.25-48-20835TBS heat transfer gauges, which are linear from 0–22 kW/m^2. The experimental heat transfer could then be compared to the similarity solution described by Liu et. al.[15] The theoretical solution is only good for a sharp cone at zero angle of attack with laminar flow.

Position	Axial Distance from Nosetip [m]	Gauge Name	Serial Number
1	0.15	SB-A	168636
2	0.19	SB-B	168635
3	0.23	SB-C	167032
4	0.28	SB-D	167034
5	0.32	SB-E	168136
6	0.36	SB-F	168633

Table 1. Axial location and serial number of the Schmidt-Boelter heat transfer gauges for the January 2011 experiments.

Figure 4 shows the TSP image of an experiment performed under quiet flow at a stagnation pressure of 131 psia and a freestream Reynolds number of 9.9×10^6/m. The SB gauges can also be seen along the model centerline as black dots. The TSP image shows a roughly uniform temperature distribution in the spanwise direction, which was expected. It also appears that the boundary layer is fully laminar since the model exhibits low, even heating. The higher heating near the nosetip is due to the thinner boundary layer. In order to implement the TSP heat transfer reduction method, the SB gauge was compared to a 5 pixel by 5 pixel patch of TSP. This surface area is similar to the sensing area of the SB gauge. The patch of TSP was chosen at the same streamwise location as the gauge, with a slightly different spanwise location. The location was chosen so that the heat transfer should be nominally the same.

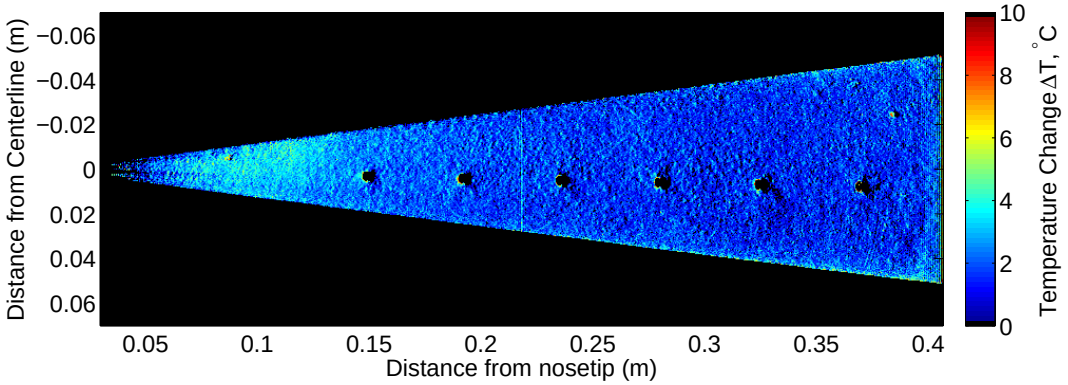

Figure 4. TSP image of the 7° half-angle cone at 0° angle of attack. $p_0 = 131$ psia, $\mathrm{Re}_\infty = 9.9 \times 10^6$/m

A plot of the data collected from sensors SB-A and SB-F, along with the heat transfer calculated at the comparison patch of TSP is shown in Figure 5. The TSP and SB data were compared at roughly $t = 0.2$ s to $t = 2$ s. Table 2 shows the values for k/L and T_{model} (from Equation 2) for sensors SB-A and SB-F. Note that there is a discrepancy between the constants, but these constants are chosen simply to fit the two data sets.

For each experiment the signals from three of the six SB gauges were amplified 100 times by three separate

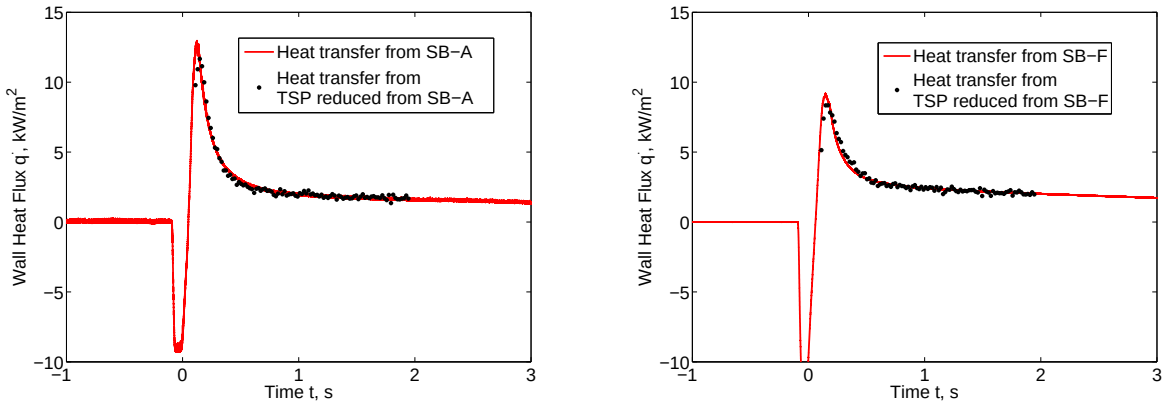

(a) SB-A (b) SB-F

Figure 5. Plot of heat transfer from the SB gauge along with the heat transfer calculated at the comparison patch of TSP.

	k/L [kW/m$^2 \cdot$ K]	T_{model} [K]
SB-A	1.16	300.9
SB-F	0.856	297.8

Table 2. Constants used in the linear fit converting the TSP temperature to heat transfer.

Stanford Research Systems SR560 low-noise voltage preamplifiers before being digitized by the oscilloscopes. The oscilloscopes were four channel Tektronix DPO7054 Digital Phosphor Oscilloscopes. The SB gauges were sampled at 50 kHz, and the scopes were operated in Hi-Res mode. In Hi-Res mode, the scope samples 8-bit data at the maximum sampling rate and averages this data in real time to obtain 12-bit data at the desired sample rate. Hi-Res mode decreases random noise and increases the vertical resolution. Before each run, the tunnel is allowed to "settle" for 10–15 minutes after filling the tunnel. The model should be in thermal equilibrium after this settling period, but the gauges typically gave a non-zero heat transfer. It was thus decided to shift the heat transfer data so that it would read 0.0 W/m^2 in the pre-run. The magnitude of this shift will be referred to as the "offset." The calibrated heat transfer is plotted along with the theoretical laminar heat transfer in Figure 6. In this figure, SB-D, SB-E and SB-F were amplified 100 times. The solid green and red lines represent the global heat transfer along the model centerline when calibrating the TSP using SB-A and SB-F respectively. Five pixels in the spanwise direction were averaged to produce the line plots. The solid squares are the heat transfer obtained from the SB gauges. The blue squares show the heat transfer with no offset subtracted, while the pink squares show the heat transfer with the pre-run offset subtracted.

Four of the six SB gauges (SB-A, SB-C, SB-D, and SB-E) are within 25% of the theoretical heat transfer when the offset is subtracted. SB-B is within 30% of the theory, and SB-F is within roughly 50% of the theory. For the three un-amplified SB gauges, the offset appears to have a significant impact on the calibrated heat transfer rates. If accurate data from the SB gauges are used to calibrate TSP to heat transfer, the results are in good agreement with theory. However, if the inaccurate data from the last SB gauge is used, the red curve shows poor agreement with theory.

The discrepancy between the reduced and theoretical data also tends to increase upstream of the first sensor. This may be due to the break down of the assumptions made to reduce Fourier's law to a linear relationship. For example, it was assumed that the base temperature was constant, but this may not be true while approaching the nosetip. Nonetheless, it appears that the new method of reducing heat transfer from the temperature-sensitive paint works well if the SB gauges provide valid measurements.

Another set of experiments during the same January 2011 entry were performed at roughly the same Reynolds number of 9.9×10^6/m to examine the effect of amplifying different SB gauges. Figure 7 shows the heat transfer from the SB gauges for four different tests, along with the theoretical heat transfer. The

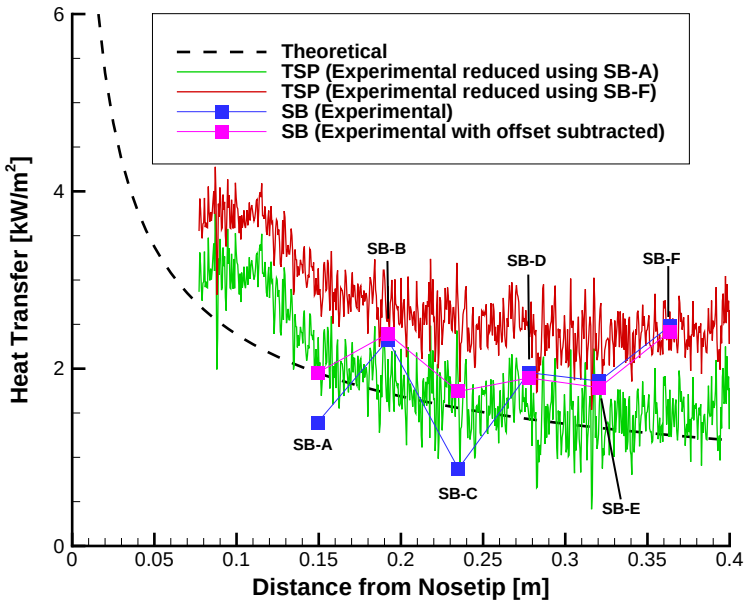

Figure 6. Heat transfer rates calculated from TSP with the reduction method and compared to theory. p_0 = 131 psia, Re = 9.9×10^6/m. SB-D, SB-E and SB-F amplified 100 times.

experimental data is all shown with the offset subtracted. Case 1 was performed with SB-D, SB-E and SB-F amplified by 100 times. Case 2 was performed with SB-A, SB-B and SB-C amplified by 100 times. Case 3 was performed with no SB gauges amplified. Case 4 was performed with only SB-B collecting data and not amplified. When the SB gauge is not amplified, subtracting the offset seems to give good agreement with the amplified gauge. Therefore, if no amplifiers are available, simply subtracting this pre-run offset seems to work well. Also note that SB-B and SB-F consistently read significantly higher heat transfer than the theory. This seems to suggest that there is some inherent error with the gauges, or that the calibration is not precise, since swapping the electronics still yields these inaccurate readings.

A new set of experiments were performed in April 2011 with some of the sensor positions swapped and some sensors replaced. This was done to see if SB-B in the previous tests would still produce inaccurate readings, and if SB-A and SB-E would still yield accurate readings. The gauges used in this set of experiments are shown in Table 3. The gauges in positions 2, 5 and 6 were the Medtherm 8-2-0.25-48-20835TBS models, which are as mentioned before are linear from 0–22 kW/m^2. The gauges in positions 1, 2 and 6 were the Medtherm 8-1-0.25-48-20835TBS models. These gauges are linear from 0–11 kW/m^2. Note that the gauges previously in positions 1, 2 and 5 (Table 1) have been moved to positions 2, 5 and 6 respectively.

Position	Gauge Name	Serial Number
1	SB-G	169256
2	SB-A	168636
3	SB-H	169251
4	SB-I	169255
5	SB-B	168635
6	SB-E	168136

Table 3. Position of SB gauges in the April 2011 experiments.

The April 2011 experiments were performed under quiet flow at a stagnation pressure of 131 psia, and a freestream unit Reynolds number of 9.9×10^6/m. Three of the six sensors appear to give accurate readings. SB-B once again shows heat transfer higher than theory. SB-E shows fairly accurate heat transfer readings

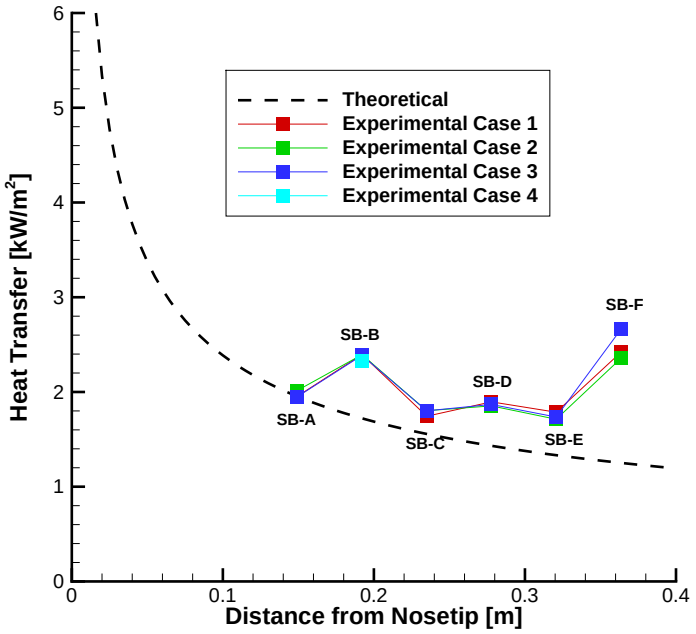

Figure 7. Heat transfer rates with different SB gauges amplified. p_0 = 131 psia, $\mathbf{Re}_\infty = 9.9 \times 10^6$/m. All data shown with offset subtracted.

during both sets of experiments. Finally, SB-A gave accurate readings in the first set of experiments, but was inaccurate in the second set. It is not clear why SB-A is inaccurate for these new experiments. In future experiments, it would be good to obtain a second calibration of the gauges, since it is possible that the factory calibration is not accurate.

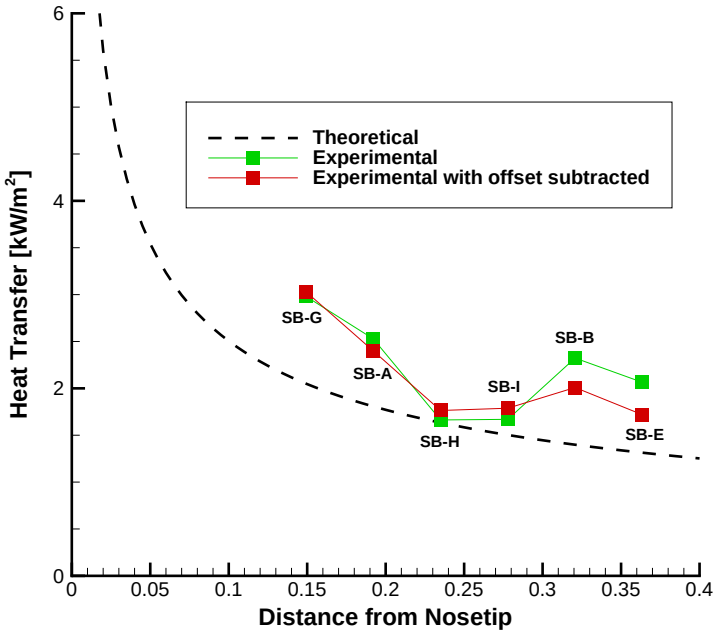

Figure 8. Heat transfer rates with SB gauge positions swapped. p_0 = 131 psia, $\mathbf{Re} = 9.9 \times 10^6$/m. SB-G and SB-H amplified 100 times.

These experiments show that the linear reduction of heat transfer from the TSP agrees well with the

theory, if the SB gauge used in the reduction process is accurate. The experiments showed that roughly half the SB gauges were within 25% of the theoretical heat transfer. Since the linear reduction method is heavily dependent on the gauge used for the calibration, it would be good in future experiments to verify the factory calibration.

III. Transition Prediction on a von Karman Ogive Geometry

Two von Karman ogive models were built for testing in the BAM6QT. The models consist of a spherical nosetip section that is tangent to a von Karman ogive geometry. The von Karman ogive is followed by a cylindrical body. These models were created to help determine if the boundary layer on a vehicle with this geometry would be laminar or turbulent at certain flight conditions. The effect of nosetip roughness on transition was also a design concern, so different nosetip roughness configurations were investigated.

A. 7.62-cm Base-Diameter Model

The first model has a base diameter of 7.62 cm (3 in.) and a length of 68 cm (26.8 in.) and four sensor ports along an axial ray. The effect of nosetip roughness was studied by using five different configurations on the 7.62-cm model: machine-finished (smooth), two-dimensional roughness strip, diamond-shaped isolated roughness elements of various heights, an array of diamond-shaped roughness elements, and a distributed roughness array.

Experiments were performed at Reynolds numbers between 10×10^6/m and 20×10^6/m under conventional noise unless otherwise specified since the quiet flow tests were laminar. Data were acquired for the 7.62-cm-diameter model using TSP, three PCB 132A31 fast pressure sensors, and a SB heat transfer gauge. Figure 9 shows the 7.62-cm model installed in the BAM6QT. The yellow region of the model is covered with TSP, while the nosetip is the unpainted aluminum. The TSP was viewed through two adjacent porthole windows designed to withstand pressures up to 300 psia. The model was tested at 0° and 2° angles of attack.

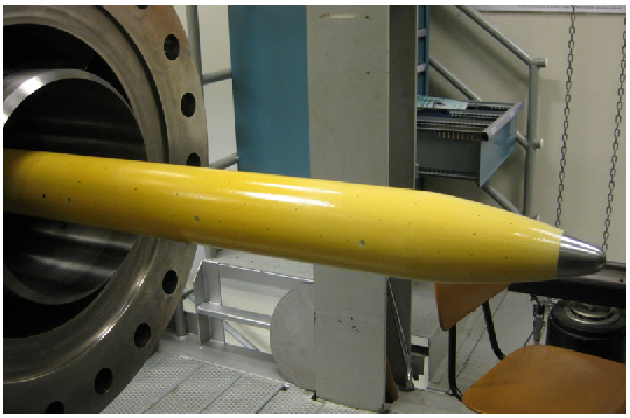

Figure 9. 7.62-cm ogive model installed in the BAM6QT.

Figure 10 shows the TSP data using the smooth nosetip at 0° angle of attack. The TSP images were reduced to a temperature change using the method described in Reference 12. Transition is usually indicated by a temperature rise that moves aft on the model as Reynolds number is decreased. While a region of higher heating was observed near the aft end of the model, this region did not move with a change in Reynolds number. The region is thought to be caused by the model bow shock reflecting off the nozzle wall and impinging on the model. The slant of the region is probably due to asymmetry in the flow. Besides the impingement of the bow shock, there is no apparent temperature rise along the model and the boundary layer appears to be laminar.

First, a 0.18-mm-tall by 1.3-mm-wide two-dimensional roughness strip was placed at the sphere-ogive junction. Later, a distributed roughness with average height of 65-μm was applied to the spherical part of the nosetip. The two-dimensional roughness strip and the nosetip with distributed roughness did not trip the model's boundary layer. When a diamond-shaped isolated roughness was installed on the nosetip at the shoulder of the spherical nose, a wedge of higher heating was observed behind the roughness (Figure 11).

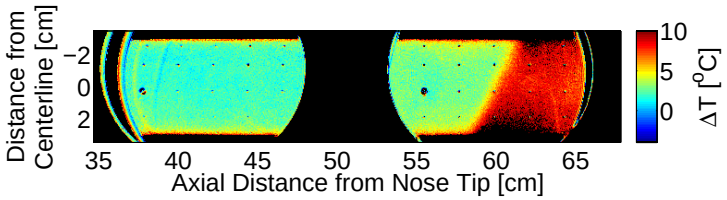

Figure 10. Smooth nosetip, 0° angle of attack, $Re = 19 \times 10^6$/m. Flow from left to right. A region of higher heating believed to be a reflected shock is seen near 60 cm from the nosetip.

This wedge typically indicates transition.[16] Increasing the roughness height widened the region of higher heating. Under quiet flow, the wedge of higher heating decreased in width and intensity, or was completely eliminated.[17]

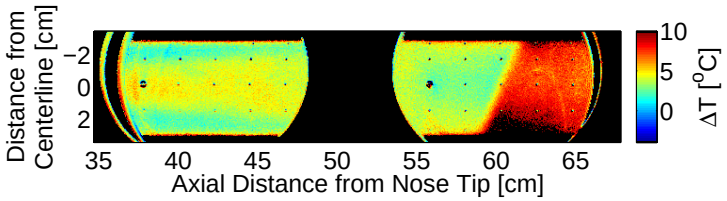

Figure 11. Isolated 51-μm roughness, 0° angle of attack, $Re = 20 \times 10^6$/m. Flow from left to right. A wedge-shaped region of higher heating can be seen as a green/yellow color in the left half of the image.

Figure 12 shows the SB gauge data for three different tunnel runs starting at about $p_{0,i} = 260$ psia ($Re = 20 \times 10^6$/m). Each of these tunnel runs used a nosetip with a different roughness configuration. The SB gauge was located 55 cm from the nosetip and can be seen as a large black dot at that location in Figures 10 and 11. The data for the smooth nosetip shows the lowest heat transfer rate, while the data for the nosetip with the large 0.25-mm (0.01-in.) isolated roughness element shows the highest heat transfer rate. At higher Reynolds numbers, the heat transfer rate behind the 51-μm (0.002-in.) isolated roughness element is similar to that behind the 0.25-mm isolated roughness element. However, as the Reynolds number decreases, the heat transfer rate drops to that seen when using the smooth nosetip. The Schmidt-Boelter gage data suggests that the smaller 51-μm roughness is causing boundary layer transition at higher Reynolds numbers ($Re > 19 \times 10^6$/m), but is not large enough to cause transition as the Reynolds number decreases.

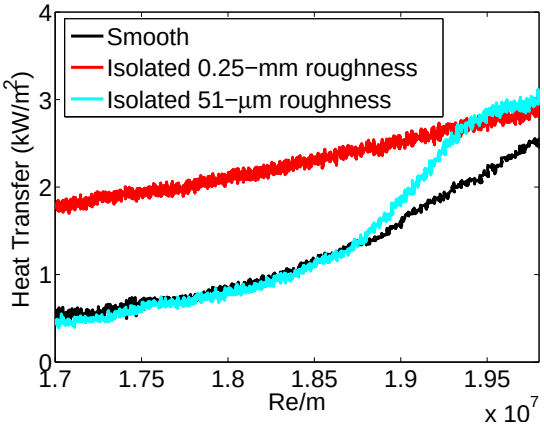

Figure 12. Schmidt-Boelter gauge data showing the variation in heat transfer rate with nosetip roughness configuration.

At 2° angle of attack, under quiet flow, hot films on the nozzle wall showed a variation in the mean level.

This variation in mean level of the hot films looked similar to that seen when boundary layer separation occurs on the nozzle wall.[7] It was therefore uncertain whether the tunnel started with the 7.62-cm model at angle of attack. A smaller 5.08-cm-diameter (2-in.-diameter) model was fabricated in an attempt to avoid starting problems and to eliminate the impingement of the reflected shock.

B. 5.08-cm Base-Diameter Model

The second model is two-thirds of the scale of the larger model and has two additional sensor ports. Three nosetips were created for this model to investigate the effect of forward- and aft-facing steps on boundary-layer transition. One nosetip was created to be nearly flush with the rest of the body, the second was scaled up to create a 0.51-mm-high aft-facing step, and the third was scaled down to create a 0.51-mm-high forward-facing step. Additionally, distributed roughness with an average roughness height of 51 μm and isolated roughness elements from 76 μm to 1.5 mm were tested on the model.

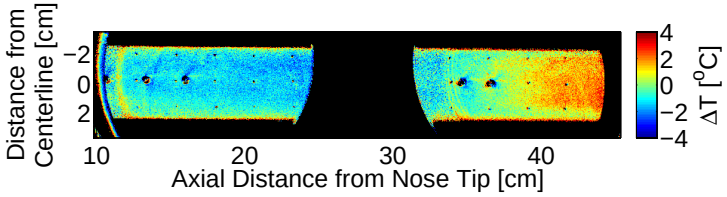

(a) $Re = 20 \times 10^6$/m.

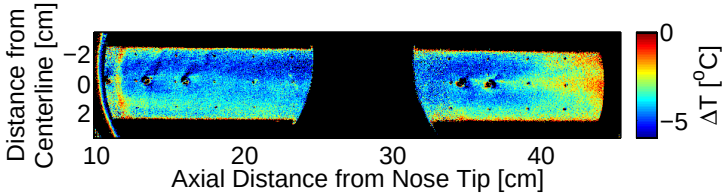

(b) $Re = 17.4 \times 10^6$/m.

Figure 13. Temperature change on the leeward side of the 5.08-cm ogive model at 2° angle of attack. Smooth, flush nosetip. Flow from left to right.

The 5.08-cm model was tested at 2° angle of attack with the flush nosetip. The TSP images showed that the reflected bow shock does not impinge on the 5.08-cm model. The nozzle-wall hot-film data also did not show indications of boundary layer separation. Additionally, a Kulite XCQ062-15A pressure transducer was mounted in the model at 36.7 cm from the nosetip to measure static pressure. It was found that the average RMS deviation in static pressure was less than 6% of the mean pressure, indicating that the tunnel started.[8]

With the smooth, flush nosetip, the boundary layer appears laminar except at high Reynolds numbers on the leeward side. At a Reynolds number of 20×10^6/m (Figure 13(a)), a region of higher heating begins near 36 cm from the nosetip. As Reynolds number is decreased (Figure 13(b)), the region of higher heating moves aft on the model, as expected because higher Reynolds numbers cause earlier boundary-layer transition.

The 0.51-mm forward-facing and aft-facing steps were tested, and the TSP data showed that neither step had a significant effect on the flow. A streamwise temperature trace was created by averaging ten pixels in the spanwise direction, at a location directly above the ray containing the sensors. A five-pixel moving-average filter was applied in the streamwise direction. The traces for the leeward side using the smooth, flush nosetip and the forward- and aft-facing steps are shown in Figure 14. Little difference is seen in the location of temperature rise due to transition for these cases, indicating that a forward- or aft-facing step of the height tested did not affect the transition location. Similar results were seen on the windward side of the model.

A distributed roughness with an average height of 51 μm was applied to the smooth, flush nosetip using a rough spray paint. Figure 15 shows the TSP data for the leeward side of the model with the distributed roughness on the flush nosetip. For a Reynolds number of 20×10^6/m (Figure 15(a)), the distributed

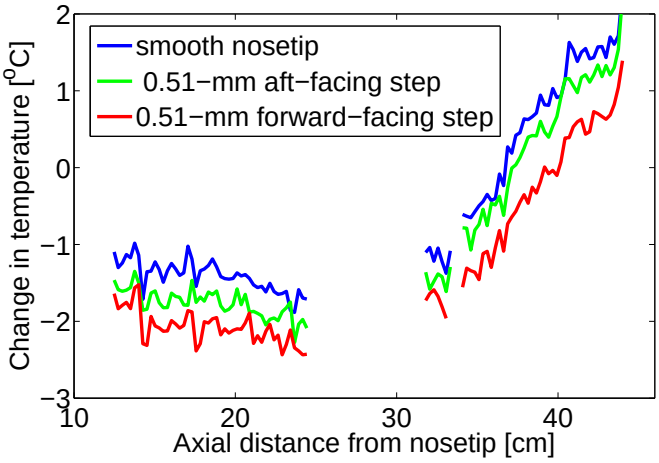

Figure 14. Axial temperature trace on the leeward side of the model for three nosetip configurations. $Re = 20 \times 10^6$/m. **Gaps in the traces are due to reflections and the lack of optical access between the porthole windows.**

roughness has caused the region of higher heating to move forward to about 20 cm from the nosetip. As the Reynolds number is decreased (Figure 15(b)), the region of higher heating moves aft on the model, as expected.

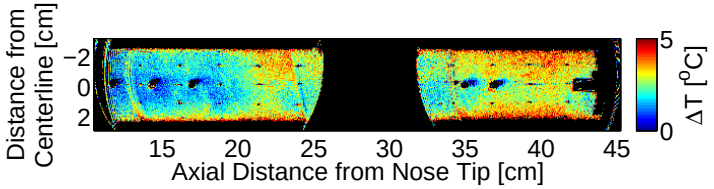

(a) $Re = 20 \times 10^6$/m.

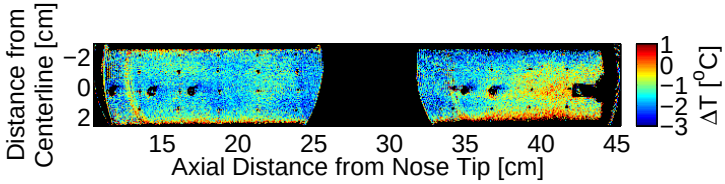

(b) $Re = 11.5 \times 10^6$/m.

Figure 15. Temperature change on the leeward side of the 5.08-cm ogive model at 2° angle of attack. Flush nosetip with distributed roughness. Flow from left to right.

Data for the SB gauge located at 35 cm from the nosetip are given in Figure 16. Data are presented in terms of $q/\sqrt{Re}$ at present because there was insufficient time to compute a non-dimensional form for heat transfer. Schmidt-Boelter gauge data for the leeward side of the model with the smooth, flush nosetip and the distributed roughness are shown in Figure 16(a). Below a Reynolds number of about 12×10^6/m, the distributed roughness has little effect. However, above a Reynolds number of 17×10^6/m, the distributed roughness configuration produces a much higher heat transfer rate than that seen with the smooth nosetip. This suggests that the distributed roughness has tripped the boundary layer, which is consistent with Figure 15.

On the windward side of the model (Figure 16(b)), the heat transfer for the distributed roughness on the

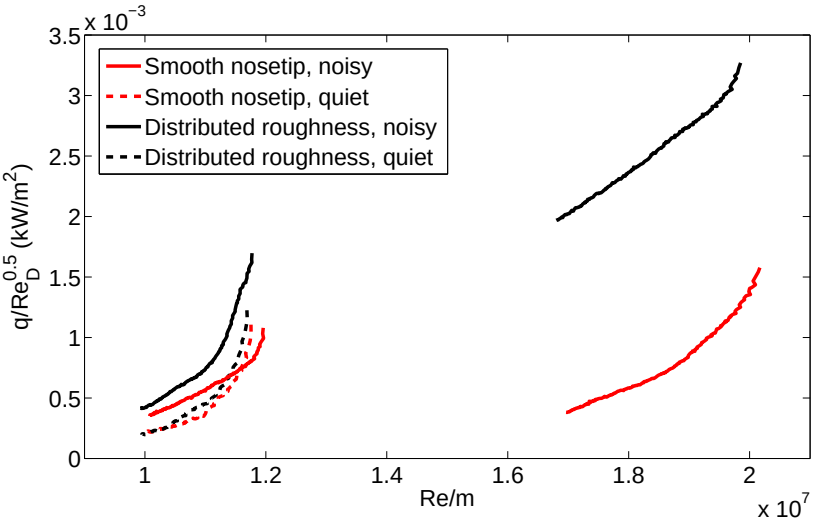

(a) Leeward Side

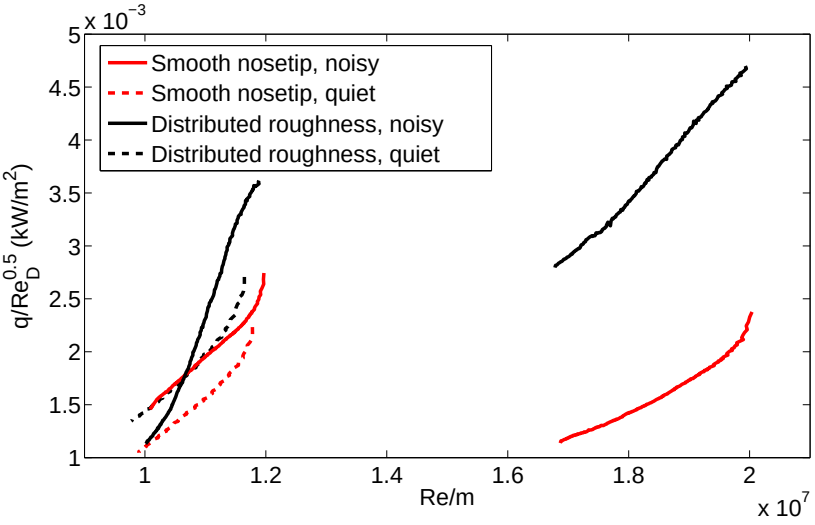

(b) Windward Side

Figure 16. Aft Schmidt-Boelter gauge data (35 cm from nosetip) for various roughness configurations.

flush nosetip begins to increase at a Reynolds number of about 10×10^6/m for noisy flow. Since the nosetip with distributed roughness did not seem to have an effect at these Reynolds numbers on the leeward side of the model, it appears that when a distributed roughness is present on the nosetip, the transition Reynolds number is lower on the windward side than on the leeward side.

An isolated roughness element on the shoulder of the ogive portion of the 5.08-cm model at 2° angle of attack created a wedge of higher heating behind the element (Figure 17). This wedge broadened in width as roughness height was increased. Additionally, the wedge was broader on the windward side of the model than on the leeward side, as seen in Figure 17. On the windward side, several distinct streamwise streaks of higher heating are apparent before they break down to turbulence.

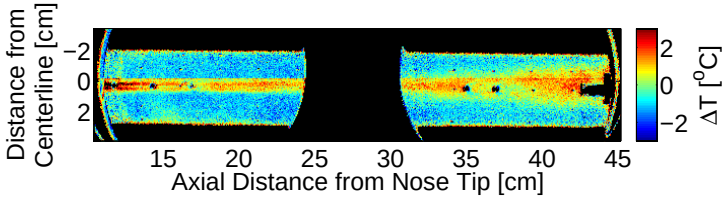

(a) Leeward Side

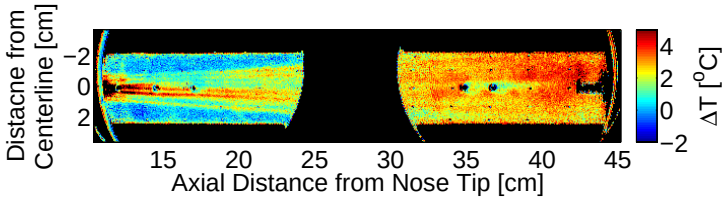

(b) Windward Side

Figure 17. Temperature change behind a 1.5-mm isolated roughness element at $Re = 11.2 \times 10^6$/m. Flow from left to right.

C. Summary

Two von Karman ogive models were tested in the BAM6QT with various nosetip roughness configurations. On the larger, 7.62-cm base diameter model, it was found that the bow shock reflected off the tunnel walls and impinged on the aft end of the model. Besides this region, when the model was tested at 0° angle of attack the boundary layer appeared laminar with a smooth nosetip, a 2D roughness strip, and distributed roughness. An isolated roughness element on the nosetip produced a wedge of higher heating behind the element, suggesting that transition occurred.

Boundary layer separation occurred on the nozzle wall with the 7.62-cm model at 2° angle of attack, and it was uncertain if the tunnel started. However, the tunnel did start with the 5.08-cm base diameter model at 2° angle of attack. Additionally, the bow shock did not impinge on the smaller model.

With the 5.08-cm model in the smooth configuration at 2° angle of attack, there was a region of higher heating on the leeward side of the model that appeared to be caused by boundary-layer transition. A 0.51 mm forward- or aft-facing step had little effect on the transition location. Distributed roughness moved the transition location forward, and appeared to cause transition at a lower Reynolds number on the windward side than on the leeward side. An isolated roughness element produced a wedge of higher heating that was wider on the windward side than on the leeward side. Much remains to be understood about instability and transition for this geometry.

IV. Measurements of Instabilities and Transition on the Compression Cone

A. Background

The compression cone is a 47-cm-long body of revolution with a 3-m circular-arc flare (Figure 18). A 0.16-mm-radius nosetip was used. This model was designed in 2009 to have high N-factors in an attempt to see natural transition in quiet flow.[6] In quiet facilities, natural transition is rarely seen due to the low maximum quiet Reynolds numbers. By creating a model with an adverse pressure gradient, the boundary layer was made to be unstable so that transition would occur earlier without the use of trips.

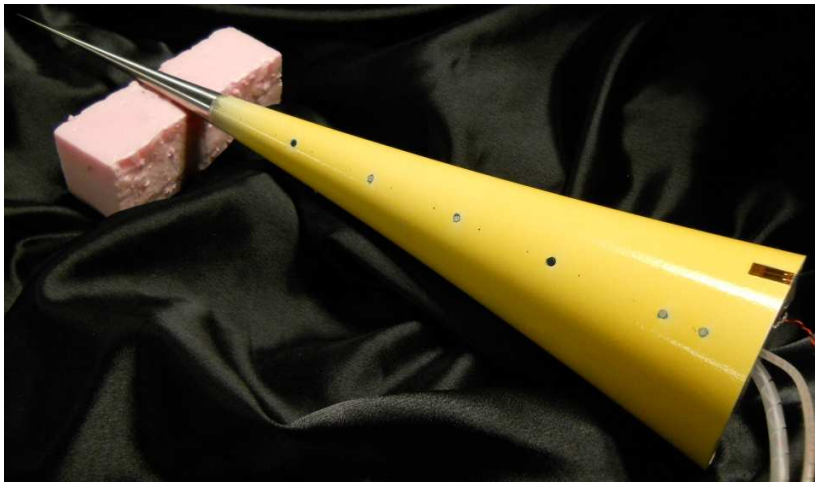

Figure 18. Compression cone model with 0.16-mm nosetip

Preliminary tests in 2009 on the 40-cm-long compression cone with a 1-mm-radius nosetip showed that an N-factor of 13 was achieved with no indication of transition.[6] After a suggestion from Balakumar that a sharper nosetip may have better receptivity,[18] the 0.16-mm-radius nosetip was created. When the model was outfitted with the 0.16-mm-radius nosetip in 2010, surprising results were achieved.[9] First, transition was seen at an N-factor of 8 under noisy flow. This is much larger than seen on other models, where $N = 4$–6.[19] Second, streamwise streaks were seen in the temperature-sensitive paints under quiet flow. These streaks appear to indicate an interaction of the dominant second-mode instability with a secondary instability.[20,21]

Further tests have been conducted on this model to provide quantitative heat-transfer measurements and to test if the spacing of the vortices can be changed using an array of small roughness elements. Efforts to calibrate temperature-sensitive paints to provide quantitative heat transfer are described in Reference 14 and Section II. A previous attempt to control the spacing of streamwise vorticity on the cone is detailed in Reference 10 and continued work on this subject is discussed in Section V.

B. Instrumentation

Six 3-mm-diameter ports exist on the model, where PCB 132A31 fast pressure transducers and Medtherm 8-2-0.25-48-20835TBS Schmidt-Boelter gauges can be interchangeably installed. These ports are located at $x = 0.23$, 0.28, 0.33, 0.38, 0.43, and 0.45 m. Four PCB 132A31 transducers and two Schmidt-Boelter gauges were installed in the model. The signals from the Schmidt-Boelter gauges were amplified 100 times using Stanford Research Systems SR560 low-noise preamplifiers. TSP was also applied to the frustum of the model as described in Section II. The paint edge was feathered in an attempt to reduce effects of the edge on the generation of instabilities. TSP data were reduced as discussed in the aforementioned section.

C. Transition in Quiet Flow

Several runs were conducted at the maximum quiet pressure of about 163 psia in an attempt to show natural transition in quiet flow. One of the indicators of transition is the shape of the power spectra of the measured surface pressure fluctuations. In Figure 19(a), sample spectra from a 7° half-angle cone with no flare is given. Here, the second mode appears as a large peak in the spectra which grows in magnitude with

downstream position. The peak frequency also decreases with axial frequency due to a thickening in the boundary layer. The second mode acts like a trapped wave in the boundary layer, so the peak frequency is inversely proportional to the boundary layer thickness.[22] At the last sensor location given in Figure 19(a), the spectra shows elevated broadband frequencies, indicating that the flow is turbulent.[23]

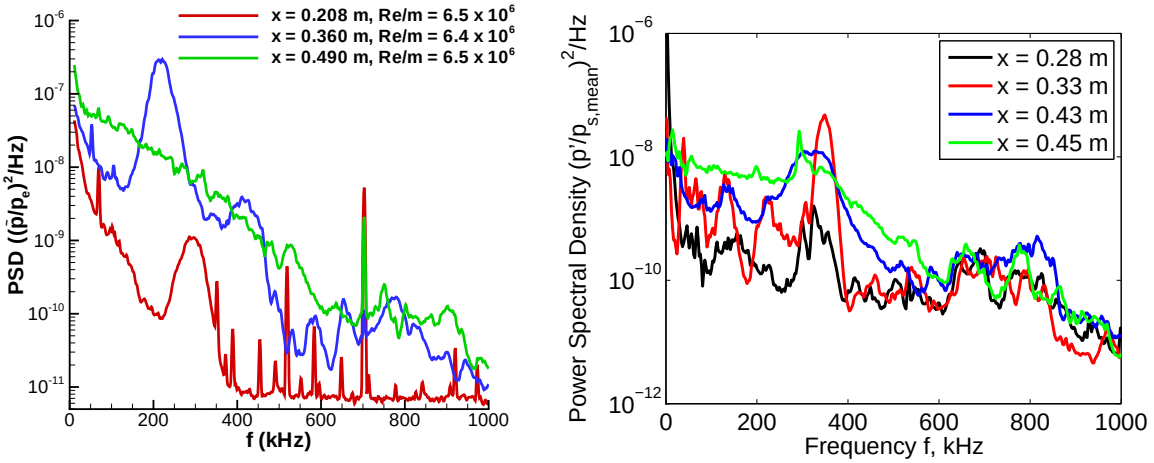

(a) 7° half-angle cone (straight, no flare).[23]

(b) Compression cone at $p_0 = 163.7$ psia, $T_0 = 151.5°$C, bleeds open.

Figure 19. Power spectra of surface pressure fluctuations on two different models.

A plot of the surface pressure fluctuations on the flared cone at the maximum quiet pressure is given in Figure 19(b). Here, the first two sensors have peaks that are centered around 300 kHz, where the second mode is expected to be. The peak frequency of the second mode does not change with axial position on this model because the boundary layer thickness is nearly constant on the flared cone. The peak is small at the first sensor location of $x = 0.28$ m. The second sensor shows a large, distinct peak, which indicates that the flow is likely still laminar at $x = 0.33$ m. These sensors are located upstream of the portion of the model shown in Figure 20, but the TSP has previously shown this region to be under laminar flow for the given conditions.[6,9,10,24] At $x = 0.43$ m, the PCB power spectrum shows a broadened peak around the second-mode wave frequencies and increased frequency content in the lower frequency range. This indicates that the flow is likely transitional at this location. Finally, at $x = 0.45$ m, the power spectrum appears to show a relatively "flat" shape, indicating that the boundary layer has become turbulent.

Previous tests have also produced images such as in Figure 20. From this image, the transition location seems to be located at the front of the second set of increased heating streaks at approximately $x = 0.41$ m. This corresponds roughly with what is seen in the pressure-fluctuation measurements. This increased heating occurs just before the PCB sensor at $x = 0.43$ m measures what looks like a "transitional" spectrum.

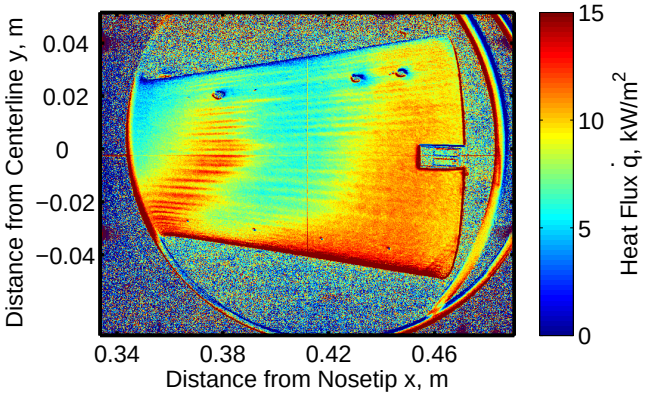

Figure 20. $p_0 = 163.7$ psia, $T_0 = 151.5°$C, bleeds open. Flow from left to right.

At these conditions, it is important to try to determine if the flow is truly quiet at the aft end of the model. If the flow is not quiet, there is a possibility that transition would occur sooner than would be seen in fully quiet flow. In previous experiments on a flared cone in the NASA Mach-6 Quiet Tunnel, the N-factor at transition was found to be 10.5.[25] This corresponded to a location outside the quiet core of the tunnel, however, and may explain why N at that facility was smaller than in the BAM6QT.

To determine whether the flow at the aft end of the cone was fully quiet, several different methods were employed. In one entry, the model was pushed far forward so that the tip of the nosetip may be in a region of non-uniform flow. The model is typically photographed in the aft porthole window of the tunnel, but for these runs, the model was photographed in the forward porthole window of the tunnel. Previous measurements of the tunnel flow characteristics in this forward position of the tunnel suggest that the flow is quiet at this location.[26] For another entry, paste-on Dantec hot films were installed on the pipe insert behind the nozzle exit at about 13 cm behind the end of the model roughly 120° apart. These were then analyzed using power spectra to attempt to quantify if the flow on the diffuser wall was quiet or noisy at this location.

1. *Effect of Model Positioning on Transition Location*

One test of whether the flow was quiet at the aft end of the model required pushing the model far forward in the tunnel. Models are typically positioned so that the back of the model is visible in the downstream porthole window, at $z_{\text{nose}} = 2.00$ m. Here, z denotes the distance from the BAM6QT nozzle throat and x is used to represent the distance from the model's nosetip. This means the aft end of the model is typically at $z = 2.47$ m, where no previous measurements of noise level have been made due to probe-access limitations. For these tests, the model was pushed forward so that the aft end was visible in the upstream porthole window, at $z_{\text{nose}} = 1.80$ m. The nosetip was thus about 20 cm forward of where the model is typically positioned in the BAM6QT, possibly in a region of non-uniform flow. However, the aft end of the model is now located at about $z = 2.27$ m (89.4 in.), where previous measurements of the tunnel flow have shown less than 0.05% noise levels.[26]

The far-forward position of the model created several nozzle-wall boundary-layer separation problems at lower pressures, so only a small portion of the data from the maximum quiet pressure could be used to compare results for the $z = 1.80$ m and 2.00 m positions. Data were taken from between about 0.6 s and 0.7 s after the tunnel started for both positions. The TSP images (Figure 21) provided similar temperature-change contours and heat-transfer contours. A comparison of streamwise cuts of the data from the runs at $z = 1.80$ and 2.00 m are given in Figure 22. Fifteen un-filtered streamwise cuts were taken on the surface of the cone and averaged together to produce a trace. The traces appear to fall directly on top of each other, indicating an agreement in data. This would appear to indicate that the heat transfer data are the same, regardless of position in the tunnel.

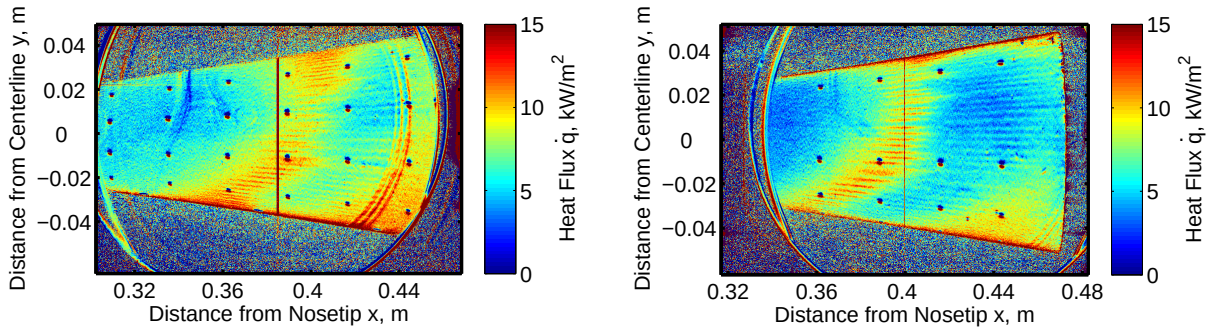

(a) $p_0 = 164.1$ psia, $T_0 = 154.9°$C, $z_{\text{nose}} = 1.80$ m

(b) $p_0 = 161.9$ psia, $T_0 = 155.4°$C, $z_{\text{nose}} = 2.00$ m

Figure 21. Comparison of temperature-sensitive paint measurements for different model positions. Flow from left to right. Vertical line down the center of images are an artifact of alignment from using 2 A/D converters.

A comparison of the pressure-fluctuation data yields similar results. However, when the model is farther aft in the nozzle exit, transition appears to be positioned in a different location. The spectra for the $z_{\text{nose}} = 1.80$ m case show what appear to be turbulent spectra at $x = 0.43$ m and 0.45 m. On the other hand, the spectra for the $z_{\text{nose}} = 2.00$ m case show what appears to be at transitional spectrum at $x = 0.43$ m

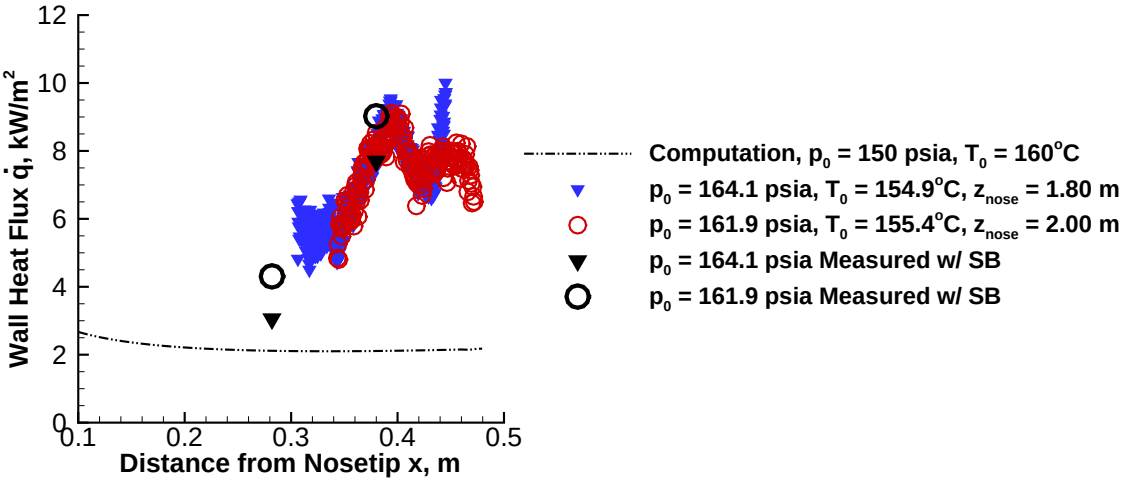

Figure 22. Comparison of streamwise cuts taken from temperature-sensitive paints images.

and a somewhat turbulent spectra at $x = 0.45$ m. It is unclear if these differences are caused by the slightly different flow conditions or the position of the model in the tunnel.

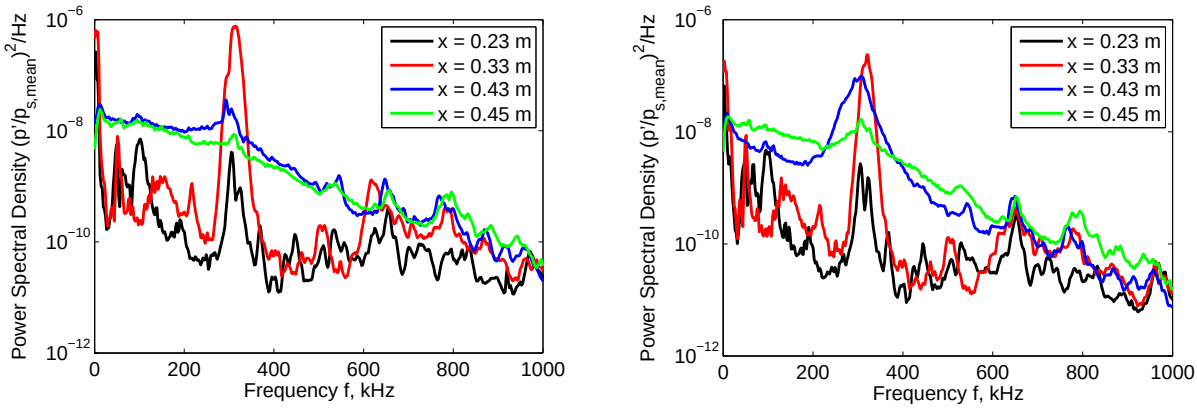

(a) $p_0 = 164.1$ psia, $T_0 = 154.9°$C, $z_{\text{nose}} = 1.80$ m

(b) $p_0 = 161.9$ psia, $T_0 = 155.4°$C, $z_{\text{nose}} = 2.00$ m

Figure 23. Comparison of power spectra for different model positions in the tunnel.

2. Hot-Film Sensors Used to Determine Flow Conditions on Diffuser Wall

At first, six Dantec type 55R47 paste-on hot films were installed in the pipe insert of the BAM6QT. Due to complications with installation and lack of open data-acquisition channels, only three hot-film sensors could be monitored during each run. A 9.5-mm (3/8-in.) gap was present in the pipe insert aft of the nozzle exit starting at around $z = 2.59$ m. These hot films were placed roughly 60° apart at $z = 2.61$ m (Figure 2), aft of the annular gap.

Some preliminary measurements were required to create a standard to which the "questionably-quiet" measurements could be compared. As these hot films could not be calibrated, it was difficult to provide a more quantitative assertion regarding the quietness of the flow. A qualitative comparison of the power spectra was used to determine if the flow was quiet on the diffuser section.

The data from three separate runs are compared in Figure 24. Data from Steen[26] are also provided for comparison. In Reference 26 (Figure 24(a)), a single hot film was placed at $z = 2.73$ m aft of a 9.5-mm (3/8-in.) gap with a pitot probe mounted at $z = 2.16$ m in the tunnel. For Figures 24(b)–(d), the compression

cone model is installed in the tunnel at around $z_{\text{nose}} = 2.00$ m. Figure 24(b) shows a run with bleeds open at a stagnation pressure of 89.8 psia and stagnation temperature of 153.2°C. At these conditions, the flow is expected to remain laminar on both the model and tunnel walls.[9,24,26–29] Figure 24(c) was done for comparison at the same conditions as Figure 24(b) with the bleeds closed. Figure 24(d) provides data at a higher stagnation pressure of 148.1 psia with the bleed valves closed. These conditions are expected to provide turbulent flow on both the tunnel wall and model.

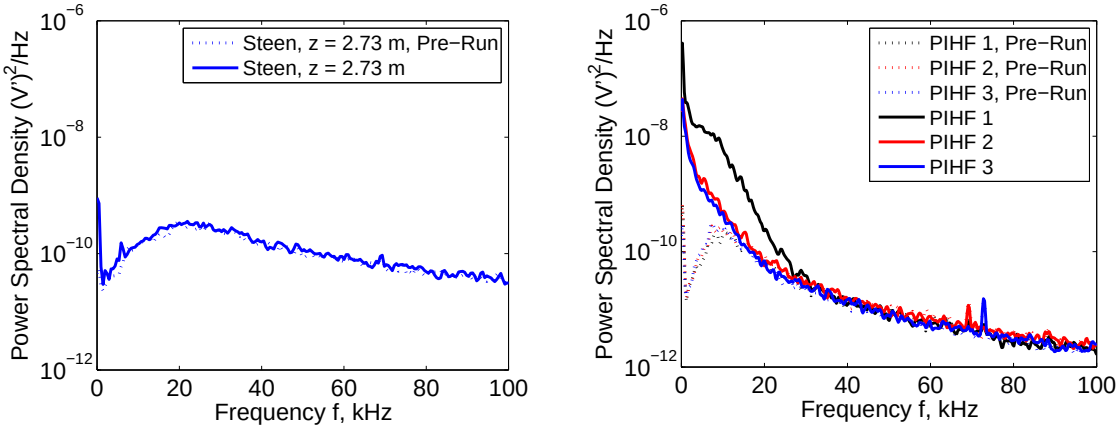

(a) Data from Steen:[26] $p_0 = 86.6$ psia, $T_0 = 156.3°$, bleeds open. Pitot probe at $z = 2.16$ m.

(b) $p_0 = 89.8$ psia, $T_0 = 153.2°$C, bleeds open. Compression cone at $z_{\text{nose}} = 2.00$ m.

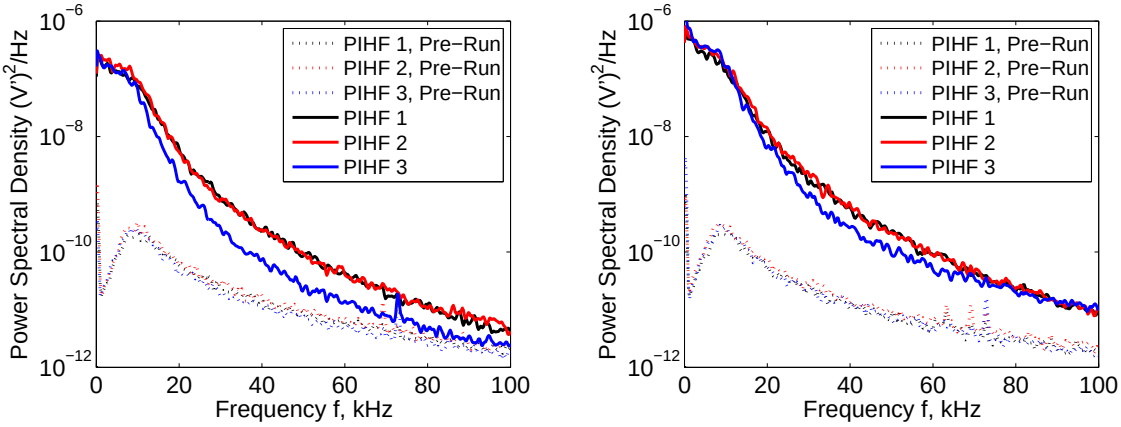

(c) $p_0 = 89.8$ psia, $T_0 = 152.7°$C, bleeds closed. Compression cone at $z_{\text{nose}} = 2.00$ m.

(d) $p_0 = 148.1$ psia, $T_0 = 152.4°$C, bleeds closed. Compression cone at $z_{\text{nose}} = 2.00$ m.

Figure 24. Power spectra of pipe-insert hot-film (PIHF) sensors for three different runs.

At first glance, the spectra with the compression cone installed in the tunnel (Figures 24(b)–(d)) all appear to show turbulent flow since the noise levels at lower frequencies are higher than in Figure 24(a). This low-frequency noise could be due to a number of reasons, such as a boundary layer tripped by the impingement of the shock on the nozzle wall or the presence of the annular gap aft of the nozzle exit. Figure 24(c) and 24(d) also have noise levels much higher than seen in Figure 24(b) at higher frequencies. Furthermore, there is a change in concavity in the power-spectral-density curve at lower frequencies for the cases that are run with bleed valves closed. The case in Figure 24(b) does not show the same characteristics, except at PIHF 1. It could be assumed that the change in concavity in the lower-frequency portion of the power spectra is indicative of some flow characteristic, though the significance is unclear.

The power spectra from the hot film at maximum quiet pressure is provided in Figure 25. This shows that the shape of the spectra is more similar to that of Figure 24(b) than to that of Figures 24(c) and (d). While there appears to be significant noise at lower frequencies, at high frequencies, noise is almost the same as the pre-run. Furthermore, there is no longer a change in concavity in the power spectra for PIHF 1, indicating that there is less noise at the lower frequencies. This was a repeatable phenomenon for higher

pressure cases with open bleed valves.

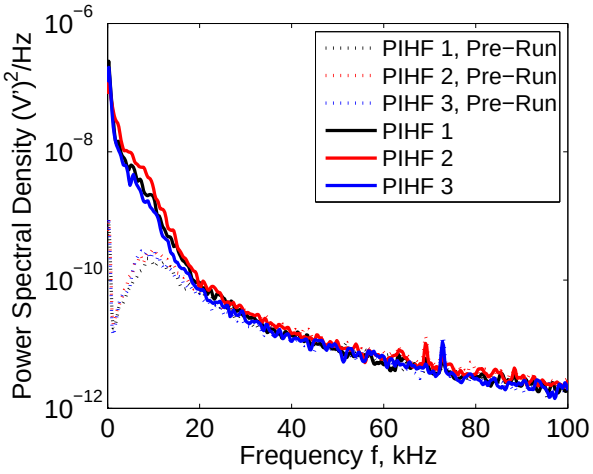

Figure 25. $p_0 = 163.7$ **psia,** $T_0 = 151.5°$**C, bleeds open. Model at** $z_{\text{nose}} = 2.00$ **m.**

While these data suggest that the flow in the diffuser section may not be quiet when a model is installed, this still does not provide conclusive evidence that transition on the compression cone does not occur in fully quiet flow. This is because the presence of a model in the wind tunnel affects the flowfield due to the presence of a bow shock. This shock impinges on the nozzle or diffuser wall and could thus affect the boundary layer of either of these sections of the tunnel. More work is needed to understand this issue.

V. Effect of Roughness Dot Spacing on the Compression Cone

Nonlinear interaction of instabilities on the flared cone mentioned in Section IV were also studied. Streamwise streaks of increased heating were seen on the cone in quiet flow at $p_0 = 140$ psia.[10] These streaks are thought to be caused by nonlinear interactions between second-mode waves and Görtler vortices. Roughness dots were applied to the cone in order to examine their effect on second-mode wave-vortex interaction.

Heat transfer was measured using SB gauges located at $x = 28$ and 38 cm on the model. TSP was used to calculate the temperature change on the surface of the model throughout the run. A Cooke Corporation pco.1600 camera was used with a 10–20 Hz frame rate, depending on the exposure time for each run. SB gauges were used to try to calibrate TSP data to provide global heat transfer as in Section II. However, these provided erroneous calibrations, so TSP data is presented only as a temperature change in this section. Possible reasons for the poor calibrations include low camera frame rate, calibrating with a SB in non-laminar flow, and poor cone alignment.

Dots were made using a new technique. Previously, dots were made by applying nail polish to the cone using a fine toothpick. In these experiments, nail polish was applied to the cone using a micro-syringe in 0.3 μL increments. For the 0.6 μL cases, 0.3 μL was applied and allowed to dry before another 0.3 μL application. This technique helped prevent dots from becoming too wide. The use of a syringe ensured a nearly uniform dot volume, but dot height and diameter varied. Dots were measured using a Mitutoyo SJ-301 Surface Roughness Tester. The typical dot diameter was 1.27 mm (0.05 in.), but some dots were up to 1.91 mm (0.075 in.) in diameter. The new technique was not as repeatable as initially hoped. The average dot height was 116 μm for 0.6 μL dots and at least 350 μm for 0.9 μL and 1.2 μL dots. Figure 26 exemplifies the variability in dot diameters. These dots were applied to a flat surface to facilitate measurement, since it is extremely difficult to use the profilometer on the complex surface of the cone.

Five different roughness dot configurations were tested as shown in Table 4. Dots were placed at $x = 35.3$ cm for all configurations and tested in the order presented in the table. Dot spacing here is defined by the number of diameters D between roughness elements, based on a 1.27 mm (0.05-in.) diameter. The stagnation pressure was roughly 160 psia and the stagnation temperature was roughly 155° C for all tests.

Temperature change along a streamwise ray was analyzed to determine the location of maximum ΔT in

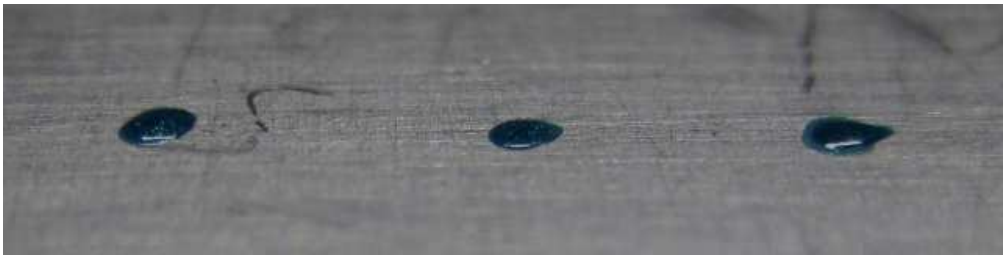

Figure 26. Photo of dots showing variation in shape for a fixed volume of 0.6 μL.

Number of Dots around Circumference	Dot Volume (μL)	Spacing between Dots	Location of Max ΔT, cm
0	—	—	40.5, 43.1
25	0.6	$4D$	35.8, 36.7
50	0.6	$2D$	36.9
100	0.6	$1D$	36.7, 37.0
100	0.9	$1D$	36.9
100	1.2	$1D$	36.6

Table 4. Roughness dot configurations.

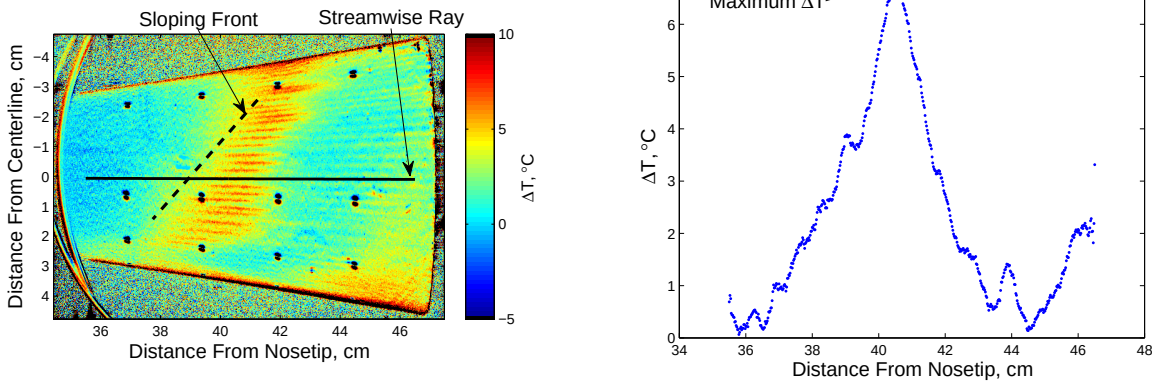

(a) Sloping streak heating front and streamwise ray.

(b) Temperature change along streamwise ray.

Figure 27. No dots, p_0 = 159.5 psia, T_0 = 155.1° C.

a streak along that ray. The forward sloping streak heating front on the cone can affect the maximum ΔT location depending on which ray of the cone is chosen for analysis, so rays near the centerline were chosen for consistency between runs. An example ray is shown as the black line in Figure 27(a). Temperature change along that ray is plotted in Figure 27(b). The data were smoothed using a moving average with a window size of 20 data points. Some configurations were tested multiple times and the locations of maximum ΔT for each run are presented.

A plot of the streamwise temperature change for the dot configurations in Table 4 is provided in Figure 28. Traces from varying the number of dots and the spacing between the dots is given in Figure 28(a). Based on these data, adding 25 dots moves the location of maximum ΔT upstream. However, the addition of more than 25 dots at this axial location does not significantly alter the maximum ΔT location from that of the 25-dot case. The effect of varying the sizes of roughness dots is given in Figure 28(b). From these data, there is little or no effect from changing dot volumes. Future tests will involve changing the location of the

roughness dots as well as the spacing and volume. Much remains to be understood regarding the nonlinear breakdown of second-mode waves on the flared cone.

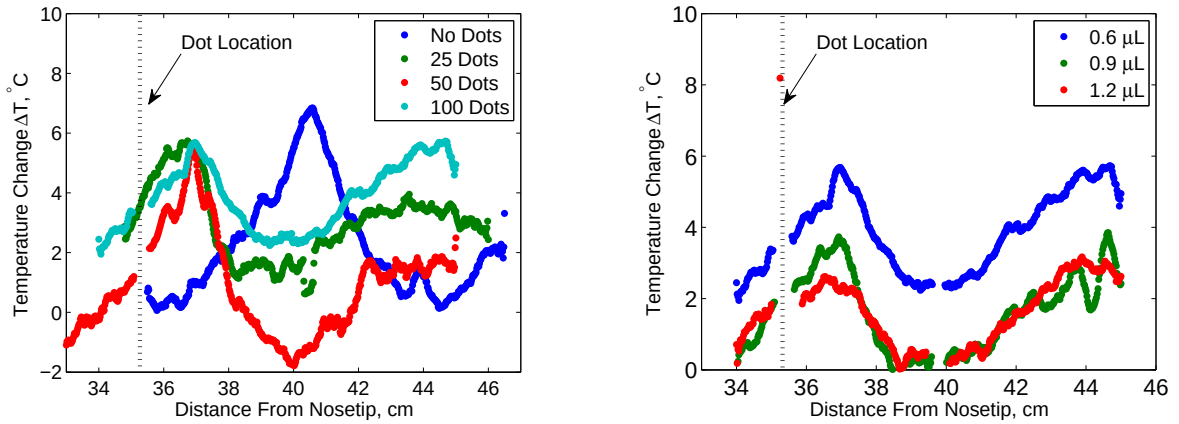

(a) Effect of changing number of dots (and spacing) around cone circumference. Dot volume is 0.6 μL.

(b) Effect of changing volume of dots for 100 dots around circumference (1D spacing).

Figure 28. Effects of different dot configurations on streamwise temperature changes.

VI. Summary

The installation of the 12-inch ball valve in April 2011 allows the BAM6QT to be started without diaphragms. The use of the ball valve to start the tunnel does not produce quasi-steady flow, but rather a linear decrease in conditions. This is due to the formation of a smoothed out expansion wave created by the slower opening of the ball valve. This development may increase the operable range of the tunnel, particularly at ranges where diaphragms are not available for use in the starting of the tunnel.

Experiments were done to validate a procedure for obtaining quantitative heat transfer from temperature-sensitive paint. The experiments were performed with a 7° half-angle cone at 0° angle of attack, where the theoretical heat transfer solution is known. The model was equipped with 6 SB heat transfer gauges, and the heat-transfer reduction procedure agreed well with the theory if the SB gauges were accurate. Only roughly half of the gauges gave accurate heat transfer readings (within 25% of the theoretical). It may be important in future experiments to obtain new calibrations since only the factory calibrations were used.

Two von Karman ogive models were constructed to study transition caused by nosetip roughness. The 7.62-cm-diameter model was tested at 0° angle of attack using a number of different rough nosetips. A smooth nosetip, and nosetips with a two-dimensional roughness strip, a distributed roughness, an isolated diamond-shaped roughness, and an array of diamond-shaped roughness elements were used. Flow on the 7.62-cm-diameter model appeared laminar for the smooth nosetip, the nosetip with a two-dimensional roughness strip, and the nosetip with a distributed roughness. An isolated diamond-shaped roughness created a turbulent wedge. The angle of this wedge grew with an increase in roughness height and either diminished or disappeared when freestream noise was reduced. The 5.08-cm-diameter ogive was constructed to provide a way to eliminate the impingement of a reflected bow shock and to allow the model to start at 2° angle of attack. Transition occurred on the leeward ray of the 5.08-cm model when the nosetip was smooth. Distributed roughness moved the transition location forward. Forward- and aft-facing steps were shown to have little effect on transition on this model.

Further tests on the 3-m circular-arc compression cone were unable to clearly show that transition occurs on the cone in fully quiet flow. Hot films were installed in the pipe insert aft of the model, but the data are unclear about whether or not flow in this section is quiet and may be affected by the impingement of the bow shock on the diffuser. Moving the model forward showed little change in the heat transfer on the surface of the model, but show some changes in the power spectra of pressure fluctuations. It is unclear if the differences in power spectra arise from changes in stagnation conditions or from positioning the model.

Different roughness configurations were also tested on the compression cone. The spacing of roughness elements does not appear to change the spacing of vortices to the spacing of roughness elements, but produces

some effect. Adding 25 dots appeared to change the location of maximum temperature change. The addition of more than 25 dots or changing the volume of the dots did not appear to affect the location of maximum temperature change. Studies of the compression cone continue.

Acknowledgments

This research is funded by AFOSR under grant FA9550-09-1-0191, by NASA under cooperative agreement NNX08AC 97A, by a Purdue fellowship, by AFRL, and by an NDSEG Fellowship. A special thanks is also given to Ed Marquart of Raytheon for providing the geometry for the von Karman ogive models.

References

[1]Lin, T. C., Grabowsky, W. R., and Yelmgren, K., "The Search for Optimum Configurations for Re-Entry Vehicles," *Journal of Spacecraft and Rockets*, Vol. 21, No. 2, 1984, pp. 142–149.

[2]Beckwith, I. E. and III, C. G. M., "Aerothermodynamics and Transition in High-Speed Wind Tunnels at NASA Langley," *Annual Review of Fluid Mechanics*, Vol. 22, January 1990, pp. 419–439.

[3]Schneider, S. P., "Flight Data for Boundary-Layer Transition at Hypersonic and Supersonic Speeds," *Journal of Spacecraft and Rockets*, Vol. 36, No. 1, January–February 1999, pp. 8–20.

[4]Schneider, S. P., "Effects of High-Speed Tunnel Noise on Laminar-Turbulent Transition," *Journal of Spacecraft and Rockets*, Vol. 38, No. 3, May–June 2001, pp. 323–333.

[5]Hofferth, J., Bowersox, R., and Saric, W., "The Texas A&M Mach 6 Quiet Tunnel: Quiet Flow Performance," AIAA Paper 2010–4794, June 2010.

[6]Wheaton, B. M., Juliano, T. J., Berridge, D. C., Chou, A., Gilbert, P. L., Casper, K. M., Steen, L. E., Schneider, S. P., and Johnson, H. B., "Instability and Transition Measurements in the Mach-6 Quiet Tunnel," AIAA Paper 2009–3559, June 2009.

[7]Juliano, T. J., Segura, R., Borg, M. P., Casper, K. M., Hannon, Jr., M. J., Wheaton, B. M., and Schneider, S. P., "Starting Issues and Forward-Facing Cavity Resonance in a Hypersonic Quiet Tunnel," AIAA Paper 2008–3735, June 2008.

[8]Gilbert, P. L., "Investigation of Downstream Suction and Starting Blunt Models in the Boeing/AFOSR Mach-6 Quiet Tunnel," Unpublished report, Purdue University, West Lafayette, IN, December 2010.

[9]Berridge, D. C., Chou, A., Ward, C. A. C., Steen, L. E., Gilbert, P. L., Juliano, T. J., Schneider, S. P., and Gronvall, J. E., "Hypersonic Boundary-Layer Transition Experiments in a Mach-6 Quiet Tunnel," AIAA Paper 2010–1061, January 2010.

[10]Ward, C. A. C., Wheaton, B. M., Chou, A., Berridge, D. C., Juliano, T. J., Gilbert, P. L., Casper, K. M., Steen, L. E., Letterman, L. E., Schneider, S. P., and Johnson, H. B., "Instability and Transition Measurements in the Mach-6 Quiet Tunnel," AIAA Paper 2010–4721, June 2010.

[11]Matsumura, S., Schneider, S. P., and Berry, S. A., "Flow Visualization Measurement Techniques for High-Speed Transition Research in the Boeing/AFOSR Mach-6 Quiet Tunnel," AIAA Paper 2003–4583, July 2003.

[12]Liu, T. and Sullivan, J. P., *Pressure and Temperature Sensitive Paints*, Springer, 1st ed., 2005.

[13]Sullivan, J. P., "Extracting Heat Transfer from TSP," Personal Communication (email), May 2010.

[14]Ward, C. A. C., *Hypersonic Crossflow Instability and Transition on a Circular Cone at Angle of Attack*, Master's thesis, Purdue University, West Lafayette, IN, December 2010.

[15]Liu, T., "Comparison of Calculated and Measured Heat Transfer in Hypersonic Laminar Flows on Cones," Unpublished Report, April 2009.

[16]Casper, K. M., Johnson, H. B., and Schneider, S. P., "Effect of Freestream Noise on Roughness-Induced Transition for a Slender Cone," *Journal of Spacecraft and Rockets*, Vol. 48, No. 3, May–June 2011, pp. 406–413.

[17]Letterman, L. E., *Instability and Transition on a von Karman Ogive in a Mach-6 Quiet Tunnel*, Master's thesis, School of Aeronautics and Astronautics, Purdue University, West Lafayette, IN, August 2011.

[18]Balakumar, P. and Kegerise, M. A., "Receptivity of Hypersonic Boundary Layers over Straight and Flared Cones," AIAA Paper 2010–1065, January 2010.

[19]van Ingen, J., "The e^N method for transition prediction," AIAA Paper 2008–3830, June 2008.

[20]Li, F., Choudhari, M., Chang, C.-L., Wu, M., and Greene, P. T., "Development and Breakdown of Görtler Vortices in High Speed Boundary Layers," AIAA Paper 2010–705, January 2010.

[21]Li, F., Choudhari, M., Chang, C.-L., and White, J., "Analysis of Instabilities in Non-Axisymmetric Hypersonic Boundary Layers over Cones," AIAA Paper 2010–4643, June 2010.

[22]Mack, L. M., "Linear Stability Theory and the Problem of Supersonic Boundary-Layer Transition," *AIAA Journal*, Vol. 13, No. 3, March 1975, pp. 278–289.

[23]Casper, K. M., *Hypersonic Wind-Tunnel Measurements of Boundary-Layer Pressure Fluctuations*, Master's thesis, School of Aeronautics and Astronautics, Purdue University, West Lafayette, IN, August 2009.

[24]Chou, A., *Characterization of Laser-Induced Perturbations and Instability Measurements on a Flared Cone*, Master's thesis, School of Aeronautics and Astronautics, Purdue University, West Lafayette, IN, December 2010.

[25]Blanchard, A. E., *An Experimental Investigation of Wall-Cooling Effects on Hypersonic Boundary-Layer Stability in a Quiet Wind Tunnel*, Ph.D. thesis, Old Dominion University, December 1995, Mechanical Engineering. NASA Report NASA-CR-198287.

[26]Steen, L. E., *Characterization and Development of Nozzles for a Hypersonic Quiet Wind Tunnel*, Master's thesis, Purdue University, West Lafayette, IN, December 2010.

[27]Wheaton, B. M., "Roughness-Induced Instability in a Laminar Boundary Layer at Mach 6," AIAA Paper 2010–1574, January 2010.

[28]Wheaton, B. M., *Roughness-Induced Instability in a Laminar Boundary Layer at Mach 6*, Master's thesis, School of Aeronautics and Astronautics, Purdue University, West Lafayette, IN, December 2009.

[29]Casper, K. M., Beresh, S. J., and Schneider, S. P., "Pressure Fluctuations Beneath Turbulent Spots in a Hypersonic Boundary Layer," AIAA Paper 2010–897, January 2011.